scientific reports

Check for updates

OPEN

Integrated multi-omics analysis and experimental verification reveal the involvement of the PI3K/Akt signaling pathway in myometrial fibrosis of adenomyosis

Qiaomei Yang[1,2,3,8], Jingxuan Hong[4,5,8], Jianhui Fu[6,8], Xianhua Liu[6], Xinye Zheng[1,2,3], Junying Jiang[1,2,3], An Zhu[7], Li Chen[1,2,3], Hao Lin[1,2,3] & PengMing Sun[1,2,3]✉

Adenomyosis (AM) is characterized as a chronic and progressive disorder with limited therapeutic strategies available. Myometrial fibrosis is a prominent pathological feature of AM, yet the underlying molecular mechanisms remain elusive. The present study conducted a comparative analysis using proteomics and metabolomics to investigate myometrial fibrosis and its underlying mechanisms. Liquid chromatography-tandem mass spectrometry (LC–MS/MS) was utilized to analyze adenomyotic and normal myometrial tissues from ten AM patients who underwent hysterectomy with myometrial fibrosis confirmed by Masson staining. This analysis established comprehensive proteomic and metabolomic profiles of AM patients and revealed widespread alterations in the proteome and metabolome within normal and fibrotic myometrium. Key proteins and signaling pathways linked to myometrial fibrogenesis were identified based on proteomic data. The integrated analysis showed significant associations between proteomic and metabolomic data and highlighted the critical role of the PI3K/AKT signaling pathway. Immunohistochemistry and Spearman's correlation analysis suggested a relationship between myometrial fibrosis and the metaplasia of myometrial stromal cells into myofibroblasts. Subsequent experiments identified crucial proteins and signaling pathways involved in myometrial fibrosis, indicating an association with the activation of the PI3K/AKT signaling pathway in myofibroblasts. Notably, PI3K/AKT inhibitors may contribute to the effective alleviation of myometrial fibrosis. This study is the first to demonstrate that myometrial fibrosis represents a critical pathological mechanism in AM through multi-omics methods and to elucidate the crucial role of the PI3K/AKT signaling pathway in this process. These findings provide valuable insights into the pathophysiology of AM and suggest antifibrotic treatment as a promising therapeutic strategy.

Keywords Adenomyosis, Multi-omics, Fibrosis, Extracellular matrix proteins, PI3K/Akt signaling pathway, Experimental verification

Adenomyosis (AM) is a non-cancerous uterine condition characterized by the aberrant infiltration of endometrial glands and stroma into the myometrium[1,2]. Clinical symptoms include heavy menstrual bleeding, severe anemia, intense dysmenorrhea, chronic pelvic pain, and infertility, as well as adverse obstetric and

[1]College of Clinical Medicine for Obstetrics & Gynecology and Pediatrics, Fujian Medical University, Fuzhou, Fujian, China. [2]Department of Gynecology, Fujian Maternity and Child Health Hospital, Fuzhou, Fujian, China. [3]National Key Clinical Specialty Construction Program of China (Gynecology), Fujian Maternity and Child Health Hospital (Fujian Obstetrics and Gynecology Hospital), Fuzhou, Fujian, China. [4]Department of Cardiology, Fujian Provincial Hospital Facilitated to Fuzhou University, Fujian Provincial Center for Cardiovascular Epidemiology Research and Prevention, Fuzhou, China. [5]Department of Cardiology, Shengli Clinical Medical College of Fujian Medical University, Fuzhou, Fujian, China. [6]Department of Pathology, Fujian Maternity and Child Health Hospital College of Clinical Medicine for Obstetrics & Gynecology and Pediatrics, Fujian Medical University, Fuzhou, Fujian, China. [7]Key Laboratory of Ministry of Education for Gastrointestinal Cancer, School of Basic Medical Sciences, Fujian Medical University, Fuzhou, China. [8]These authors contributed equally: Qiaomei Yang, Jingxuan Hong and Jianhui Fu. ✉email: sunfemy@hotmail.com

neonatal outcomes, all significantly impacting patients' quality of life[2,3]. Epidemiological studies suggest that the incidence of AM ranges from 6 to 10% among women of reproductive age, increasing to 60% among infertile women[4]. Unfortunately, effective conservative treatments are absent for most AM patients, often leading to hysterectomy, despite its permanent implications for fertility and the substantial economic burden on individuals and society[5,6]. These challenges are closely linked to previous studies' limitations in fully elucidating the precise molecular mechanisms underlying AM development[7], particularly the fibrosis of the myometrium following endometrial tissue invasion[8,9]. Therefore, a comprehensive approach is urgently needed to enhance our understanding of the complex myometrial pathogenesis of AM.

With advancements in molecular biology and bioinformatics, high-throughput omics technologies are increasingly utilized to identify disease biomarkers, understand biological mechanisms, and monitor disease progression[10,11]. Several proteomic studies of AM based on the myometrium, serum, and extracellular vesicles have identified proteins such as ANXA2, LASP1, HSP90A, STIP1, TAGLN-2, COX-2, IFITM3, and SFRP4, as well as highlighted biological pathways including ANXA2/HIF-1α/VEGF-A, inflammatory response, regulation of apoptosis, cell adhesion, and immune response, which are closely associated with AM progression and may guide future research on mechanisms and drug development targets[12–18]. Metabolomics studies are even rarer; Bourdon et al. investigated the serum metabolome of AM patients using proton nuclear magnetic resonance (1H-NMR) and found that the changes in AM metabolite levels mainly involve immune activation, cell proliferation, and migration[19]. Song et al. performed a metabolomic analysis of myometrium tissue from AM and non-AM patients and found that inflammation, oxidative stress, cell proliferation, apoptosis, and energy metabolism are involved in AM progression[20]. Furthermore, Chen et al. identified sixty differentially expressed metabolites in intestinal metabolites, primarily related to steroid hormone biosynthesis and various amino acid metabolism in AM mice[21]. The integrated multi-omics analysis facilitates the simultaneous exploration of biological regulatory mechanisms at gene, protein, and metabolic levels, yielding a more systematic and comprehensive understanding of life processes than single-omics analyses for elucidating gene function, phenotypic effects, subsequent molecular mechanism models, and practical applications[22–24]. However, no multi-omics analysis exists investigating the mechanisms underlying uterine lesion occurrence and progression in AM.

The PI3K/AKT signaling pathway, which is widely present in cells and plays a significant role in various cellular processes, including cell survival, growth, proliferation, angiogenesis, metabolism, and migration[25], may play a pivotal role in uterine smooth muscle cell proliferation and epithelial proliferation in AM[26,27]. Research-based on network pharmacology indicates that PI3K/AKT is activated in AM rat models, which is involved in upregulating Bcl-2 expression[28]. The PI3K/AKT signaling pathway is also considered a critical node and master regulator during fibrogenesis. Targeted inhibition of this pathway is being explored as a potential therapeutic strategy to mitigate idiopathic pulmonary fibrosis progression[29]. For instance, Icariside II exerts significant anti-idiopathic pulmonary fibrosis via inhibiting the PI3K/Akt/β-catenin signaling pathway based on ameliorating myofibroblast activation[30]. Chronic restraint stress alleviated liver fibrosis in mice through upregulation of the INSR/PI3K/AKT/AMPK pathway[31]. Fufang Shenhua tablet inhibits renal fibrosis by inhibiting the PI3K/AKT signaling pathway[32]. However, the role of the PI3K/AKT signaling pathway in myometrial fibrosis associated with AM has yet to be elucidated.

This study is the first to utilize LC–MS/MS to integrate proteomics and metabolomics analysis of myometrial tissue from patients with AM. The objectives were to investigate the fibrotic molecular mechanisms, mainly focusing on fibrosis formation, progression, and metabolic characteristics within myometrial lesions. Adenomyotic and normal myometrium samples were obtained from the same uterus to ensure consistency. Based on comprehensive omics and experimental methods, this study aimed to elucidate the role of the PI3K/AKT signaling pathway in the pathogenesis and progression of fibrosis in the myometrium of AM. This research provides a foundational basis for improving the clinical management of AM.

Materials and methods

Study design and patients

Ten pairs of fresh myometrial tissue samples, with and without adenomyotic lesions, were collected from AM patients who underwent hysterectomies at Fujian Provincial Maternity and Children's Hospital, affiliated with Fujian Medical University, between 2022 and 2023. The study was approved by the Fujian Provincial Maternity and Children's Hospital (Approval No. 2023KYLLRD01030) and adhered to the Declaration of Helsinki and relevant guidelines. All participants provided informed consent. Magnetic resonance imaging (MRI) was utilized as AM's initial clinical diagnostic method. Postoperative histopathological examination of the uterine specimens further confirmed the diagnosis. Clinical data were collected via a detailed questionnaire, including age, menarche age, gravidity, parity, serum CA125 levels, and MRI. Dysmenorrhea was evaluated using a Visual Analog Scale (VAS) into four levels: no dysmenorrhea (0), mild (1–3), moderate (4–6), and severe (7–10). Menstrual blood loss was assessed using a pictorial blood assessment chart (PBAC). A PBAC score exceeding 100 signifies a blood loss greater than 80 ml, indicating heavy menstrual bleeding. Patients who had spontaneous menstruation within the six months before surgery and had not undergone hormonal therapy were included. Those with endometriosis, certain cancers, tumors, diabetes, hypertension, or thyroid diseases were excluded. Uterine volume (V) was calculated using the formula V (cm^3) = length × width × height × 0.523, with values exceeding 350 cm^3 classified as enlarged[33]. The study flow is illustrated in Fig. 1.

Hematoxylin and eosin (H&E) staining

H&E staining was utilized to examine histological changes. Following dewaxing and hydration, sections were stained with hematoxylin for 15 min, rinsed, and then stained with eosin for 7 min. After a subsequent rinse, they were dehydrated, mounted, and examined for digital imaging under a light microscope (BX-41, Olympus).

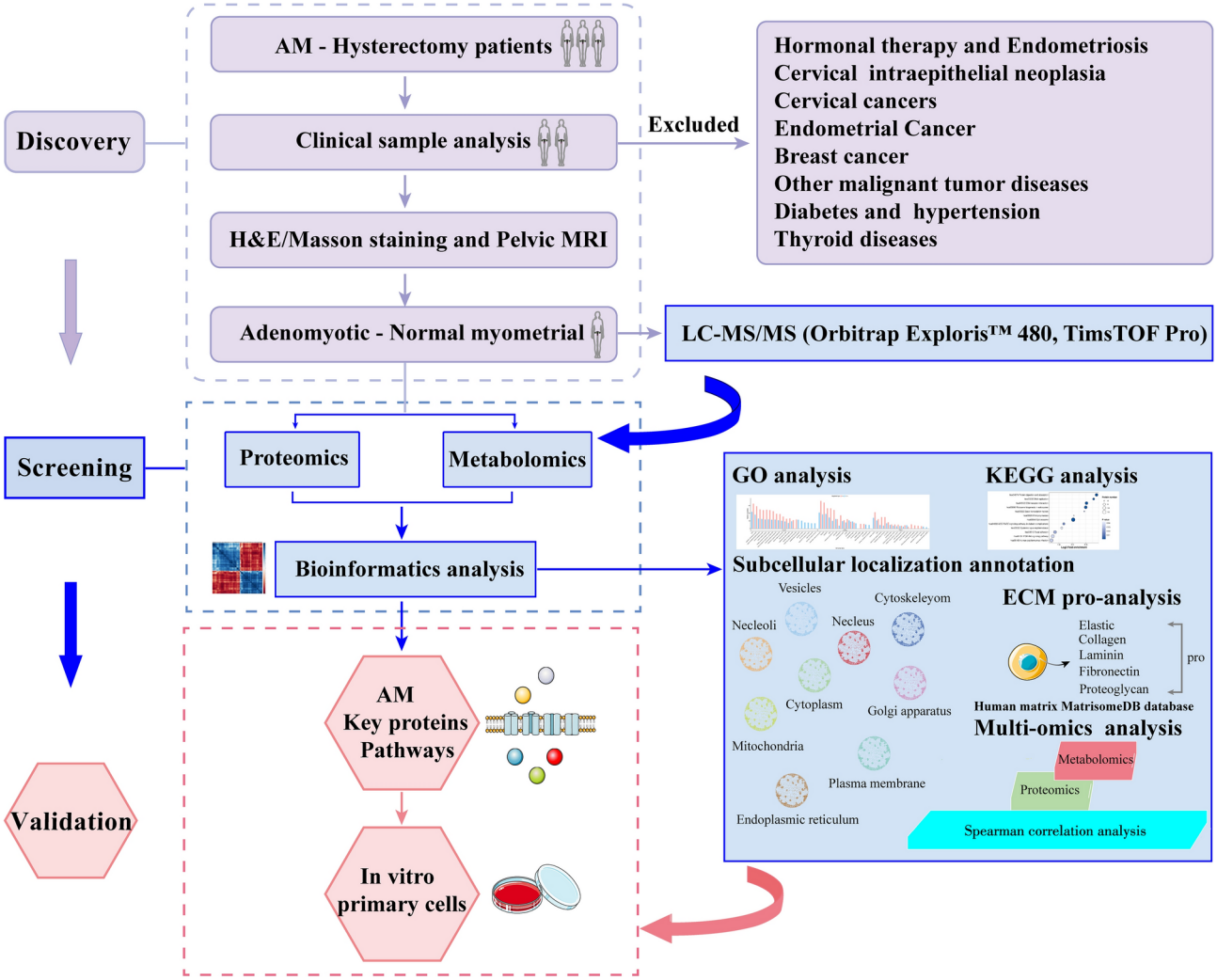

Fig. 1. Flow chart in our study.

This method also serves as the gold standard for diagnosing AM, ensuring the accuracy of specimen selection for subsequent omics experiments. The presence of endometrial glands and stroma within the myometrium observed under microscopy definitively established the diagnosis.

Masson's trichrome staining

Tissue sections were dewaxed in xylene, rehydrated, soaked in 2.5% potassium dichromate overnight, then rinsed with distilled water. The nuclei were counterstained with hematoxylin for 1 min and differentiated in 1% acid alcohol. Fibrous tissue was stained with Lichun red magenta for 6 min, followed by differentiation in phosphomolybdic acid for 1 min. Subsequently, the sections were briefly stained with aniline blue, dehydrated, sealed with neutral resin, and cover-slipped for examination under a light microscope (BX-41, Olympus).

Proteomics analysis

Protein extraction

The tissue samples were pulverized into cell powder and then lysed using a lysis buffer. The lysate underwent high-intensity ultrasonic processing three times on ice with a Scientz ultrasonic processor from Zhejiang, China. Following centrifugation at 12,000*g* and 4 °C for 10 min, the supernatant was collected, and protein concentration was determined using a BCA assay per the manufacturer's instructions.

Preprocessing for LC–MS/MS analysis and database search

An equal amount of protein sample was combined with pre-cooled acetone, followed by vortexing for thorough mixing. Subsequently, four times the volume of pre-cooled acetone was added, and precipitation was carried out at − 20 °C for 2 h. The precipitate was obtained by centrifugation at 4500*g* for 5 min. The supernatant was discarded, and the precipitate was washed three times with pre-cooled acetone. After drying, the precipitate was reconstituted in TEAB at a final concentration of 200 mM and subjected to ultrasonic dispersion. Trypsin was added at a trypsin-to-protein mass ratio of 1:50 for overnight digestion. The sample was reduced with 5 mM

dithiothreitol at 37 °C for 60 min and subsequently alkylated with 11 mM iodoacetamide in the dark at room temperature for 45 min. Peptides were then purified using the Strata X solid-phase extraction column on a nanoElute UHPLC system (Bruker Daltonics). LC–MS/MS analysis was performed on an Orbitrap Exploris™ 480 (ThermoFisher Scientific) mass spectrometer. The MS/MS data were processed using the MaxQuant search engine (v.1.6.15.0)[34] and reviewed against the human SwissProt database (20,422 entries). The mass spectrometry proteomics data have been deposited to the ProteomeXchange Consortium via the PRIDE partner repository with the dataset identifier PXD058989.

Differential proteins function annotation, classification, and enrichment analysis
The Eggnog-mapper software (v2.0), based on the EggNOG database, was employed for gene ontology (GO) annotation and functional classification analysis[35]. KEGG pathway annotation and functional classification analysis were conducted using the KEGG pathway database[36]. Additionally, subcellular localization of the proteins was annotated using WoLF PSORT software and predicted and analyzed with PSORTb software (v3.0). The human matrix MatrisomeDB (https://matrisomedb.org) was also used to annotate and identify matrix body proteins[37]. Annotations were performed on differentially expressed proteins (DEPs) with a |log2 fold change (FC)| ≥ 1.5 and $p < 0.05$. GO enrichment analysis[38] and KEGG pathway analysis[39] were conducted to identify significant GO terms and pathways associated with DEPs, with a significance threshold of $p < 0.05$.

Metabonomics analysis

Sample preparation for metabolomic analysis
Following the proteomic analysis, samples were retrieved from − 80 °C storage, weighed, and ground into powder using liquid nitrogen in a mortar. Each group was treated with a quadruple MeOH/ACN buffer (1:1, v/v), vortexed, and sonicated for lysis. Subsequently, samples were sedimented at − 20 °C for 1 h, then centrifuged at 18,000*g* for 15 min at 4 °C to remove cell debris and protein precipitates. The resulting supernatant was transferred to a new tube. After concentration, the insoluble fraction was resuspended with an equal volume of ACN: H_2O (1:1, v/v) and centrifuged again. Samples designated for metabolomics were prepared and stored at − 80 °C until LC/MS analysis.

Metabolomic LC–MS analysis
Metabolites were extracted for LC–MS analysis using a 1.7 μm particle-size, 2.1 mm × 100 mm ACQUITY UPLC BEH C18 Column (Waters, Milford, MA, USA) for separation. The injection volume was 10 μL, and elution was conducted at a constant flow rate of 400 μl/min with a column temperature of 40 °C. The mobile phase comprised water with 0.1% formic acid (A) and acetonitrile containing 0.1% formic acid (B). Elution gradients were programmed as follows: 2–98% B for 11 min, 98% B for 1 min, 98–2% B for 0.1 min, and 2% B for 2.9 min. Subsequently, metabolites were introduced into an electrospray ionization (ESI) source and analyzed by timsTOF Pro (Bruker, Karlsruhe, Baden-Württemberg, GER) mass spectrometry. The ESI voltage was maintained at 4.5 kV, and the mass spectrometry scan range was set at 50–1300 m/z. The data acquisition mode was the Parallel accumulation-serial fragmentation (PASEF) mode.

Metabolomics data analysis
Peak extraction, alignment, and retention time correction of the raw data were executed using MetaboScape 2022 (Bruker, Karlsruhe, Baden-Württemberg, GER). Mass errors were controlled within 20 ppm to ensure the accurate identification and structural and annotation information of metabolites was obtained by comparing spectra with the NIST Chemistry WebBook (NIST)[40], Human Metabolome Database (HMDB)[41], personnel database, and public databases. Quantitative metabolite information from database matching was used to calculate fold change in metabolite expression between the two groups. Significantly differentially expressed metabolites (DEMs) were determined using the variable importance in the projection (VIP) values, which combined the p-value from t-test analysis with multivariate statistical analysis using orthogonal partial least squares-discriminant analysis (OPLS-DA). The magnitude of between-group variation and within-group variability was visualized using Principal Component Analysis (PCA) plots. KEGG fold enrichment of DEMs was conducted using the KEGG database[39]. Statistical threshold set at fold change > 1.5, p-value < 0.05, and VIP values ≥ 1. Metabolomics data have been deposited to the EMBL-EBI MetaboLights database with the identifier MTBLS11965.

Proteomics and metabolomics integrated analysis

We conducted an integrated analysis of proteomics and metabolomics data to elucidate the molecular mechanisms underlying diseases or external stimuli and understand the regulatory effects of various omics on pathways. We identified differentially expressed proteins (DEPs) and metabolites (DEMs) and mapped them onto iPath global metabolic pathways. A Spearman correlation analysis was performed to construct a correlation network of these DEPs and DEMs. Utilizing the Metscape plugin in Cytoscape, we analyzed proteome and metabolome interaction networks[42]. To further explore specific pathway interactions associated with fibrosis, we conducted a focused Spearman correlation analysis on DEPs within the PI3K/AKT signaling pathway and their corresponding DEMs to uncover potential regulatory mechanisms[43].

Western blotting assay

Myofibroblasts and myometrial tissues underwent protein extraction. Proteins were separated by 10% SDS-PAGE with 25 μL of total protein per sample, transferred to PVDF membranes, and blocked with 5% BSA for 1 h at room temperature. After washing with TBST, membranes were incubated overnight at 4 °C with primary antibodies: anti-Collagen IV, anti-p-PI3K, anti-PI3K, anti-AKT, anti-p-AKT, anti-FN1, anti-STK11,

anti-HMGB3, anti-SFRP4, anti-MYH9, and anti-β-actin as a loading control. They were then incubated with HRP-conjugated secondary antibodies for 1 h and washed with TBST. Chemiluminescent signals were detected using an ECL kit on a Chemiluminescence Imaging System, analyzed with ImageJ, and plotted using GraphPad.

Immunohistochemical (IHC) assay

Tissue slides were dewaxed in xylene for 30 min, rehydrated, and incubated overnight at 4℃ with primary antibodies: anti-CD10, anti-caldesmon, anti-α-SMA, anti-FN1, anti-AKT, and anti-p-AKT. After washing, slides were incubated for 2 h with goat anti-mouse or goat anti-rabbit IgG secondary antibodies. DAB chromogen was used to visualize reactions, and results were scored semiquantitatively based on positive cell percentage and staining intensity[44]. Caldesmon and α-SMA staining was observed in the stroma and smooth muscle tissues, but only the stromal part was evaluated. To reduce bias, two independent pathologists assessed all samples.

Cell culture

We carried out the isolation and culture of adenomyosis-derived primary myofibroblasts. Briefly, adenomyosis lesions from patients were rinsed with PBS, minced into small pieces of approximately 1 mm^3, and treated with 10% collagenase IV for 2 h. The samples were filtered through a 30 μm cell strainer, and the cell suspension was centrifuged at 300*g* for 7 min. The cells were grown in T25 flasks with 5 mL of DMEM, supplemented with 10% FBS, 1% penicillin/streptomycin, and 1% L-alanyl-L-glutamine. When cell density exceeded 80%, they were passaged. Trypsin was added, and the flasks were incubated at 37 °C for 4 min. Digestion was halted with complete medium once 80% of the cells detached. The suspension was centrifuged at 300*g* for 4 min. The cells were resuspended in 1 mL of fresh medium and plated into a new dish at a 1:2 dilution. The cells were cultured in a humidified incubator with 5% CO_2 at 37 °C.

Immunofluorescence(IF) assay

Cells were seeded onto slides in 24-well plates at 80,000 cells per well, fixed with 4% paraformaldehyde for 15 min, and washed with PBS. A 5% BSA blocking solution was applied for 20 min at 4 °C, followed by two PBS washes. Sections were incubated overnight at 4 °C with primary antibodies: anti-CD10, anti-caldesmon, and anti-**α**-SMA. The next day, the slides were washed twice and incubated for one hour with secondary antibodies. Hoechst 33342 (Beyotime) was utilized for nuclear staining of the cells.

5-ethynyl-2-deoxyuridine(EdU) Assay

Cells were seeded into 24-well plates containing cell slides at a density of 80,000 cells per well and treated with PI3K/AKT-IN-1 (HY-144806, MCE) for 48 h. DNA synthesis was measured using the Click-iT EdU Cell Proliferation Kit (C0071S, Beyotime) as per the manufacturer's instructions.

Statistical analysis

The normality of variables was assessed using the Shapiro–Wilk test. Continuous data are presented as mean ± standard deviation (SD), while dichotomous data are reported as n (%). As deemed suitable for the analysis, descriptive statistics were compared using appropriate statistical tests, including the Student's t-test, Mann–Whitney U test, Chi-squared test, and Fisher's exact test. Pearson's or Spearman's rank correlation coefficient was used to evaluate correlations between two variables, depending on whether both were continuous or at least one variable was ordinal. Statistical analyses were conducted using R Studio software, with the significance level at $p < 0.05$.

Results

Clinical data analysis

Demographic data for the 10 AM patients are presented in Table 1. The patients ranged from 39 to 54 years old, with a mean of 46.5 ± 3.14 years. The data reveals a high prevalence of multiparity and multigravidity, with 70% (7/10) having a parity of ≥ 2 and gravidity of ≥ 3. Dysmenorrhea was a significant symptom, especially among patients with elevated serum CA125 levels (> 35 IU/L); all 8 such patients reported dysmenorrhea, with 75% (6/8) experiencing severe discomfort and 25% (2/8) experiencing moderate discomfort. Regarding menstrual volume, 70% (7/10) had an increase, with 85.7% (6/7) of these patients exhibiting elevated CA125 levels. Uterine enlargement was noted in 80% (8/10) of patients, with 87.5% (7/8) also having high CA125 levels. These findings highlight a strong link between elevated CA125 levels, dysmenorrhea, increased menstrual volume, and uterine enlargement in adenomyosis.

MRI of AM revealed a blurred boundary between the deep and superficial layers of the myometrium, characterized by uneven signal intensity and scattered high-signal lesions within the adenomyotic tissue (Fig. 2A). Gross examination revealed a thickened, hardened myometrium with enlarged muscle fibers and small spaces containing dark red or blue-purple fluid in adenomyotic myometrium (Fig. 2B). H&E staining showed endometrial glands and stroma invading the myometrium with hyperplastic and irregular shapes (Fig. 2C), while Masson staining demonstrated myometrial fibrosis around the adenomyotic lesion (Fig. 2D).

Proteomics analysis

To better investigate the composition and differences of proteins in normal myometrium and fibrotic adenomyotic myometrium of AM, we conducted a four-dimensional(4D) label-free proteomic analysis based on an LC–MS/MS approach. Pearson's correlation coefficient (PCC) in Fig. 3A and principal component analysis (PCA) in Fig. 3B were used to assess sample repeatability, demonstrating the statistical consistency of quantitative results from 10 biological replicates. Supplementary Fig. S1A–F further confirmed the high accuracy and reliability of the mass spectrometry detection.

Clinical features	Overall population	No. of cases n(%)
Mean age (range), years	46.5 ± 3.14	
	39–45	3 (30)
	46–54	7 (70)
Age at menarche (range), years	13.7 ± 1.64	
	11–13	3 (30)
	13–16	7 (70)
The level of serum CA125	< 35 IU/L	2 (20)
	> 35 IU/L	8 (80)
Menstrual cycle	Proliferative period	7 (70)
	Secretory period	3 (30)
Gravidity	≤ 1	1 (10)
	2	2 (20)
	≥ 3	7 (70)
Parity	≤ 1	3 (30)
	≥ 2	7 (70)
Dysmenorrhea (score)	No/mild	1 (10)
	Moderate	2 (20)
	Severe	7 (70)
Menstrual volume (ml)	Normal	3 (30)
	Increscent	7 (70)
Uterine volume ($\overline{x} \pm SD$), cm^3	342.32 ± 181.12	
	Normal	2 (20)
	Increscent	8 (80)

Table 1. Clinical features of patients with adenomyosis.

DEPs between the adenomyotic myometrium group (AM) and the normal myometrium group (control) were presented in Fig. 3. Clustering analysis of all identified proteins revealed significant expression differences between the AM and normal control groups (Fig. 3C). A total of 6013 proteins were identified, with 5193 included in the comparative analysis. 654 DEPs were identified, with 403 upregulated and 251 downregulated (Fig. 3D). The most prominent DEPs are illustrated in Fig. 3E. GO and KEGG pathway annotation analyses highlighted the potential functional roles of these DEPs, including involvement in intracellular anatomical structures, organelles, regulation of biological processes, signal transduction, and the immune system, as depicted in Fig. 3F,G.

Subsequently, we conducted an enrichment analysis on the DEPs. The KEGG pathway cluster analysis identified significant pathways, including complement and coagulation cascades, ECM-receptor interaction, PI3K-AKT signaling pathway, cell adhesion molecules, and TGF-β signaling pathway (Fig. 4A). The most strongly enriched gene sets of upregulated pathways were the PI3K/AKT signaling pathway and the ECM-receptor interaction active in wound healing and fibrosis but also included gene sets representing inflammation, cell proliferation, endometrial and interstitial invasion, and metabolism (Fig. 4B). Furthermore, GO enrichment results demonstrate that the DEPs are primarily enriched in biological processes such as rRNA metabolic process, rRNA processing, and RNA metabolic process. They are predominantly involved in molecular functions, including extracellular matrix structural constituent, serine-type endopeptidase inhibitor activity, and catalytic activity. They are mainly localized in cellular components such as the cytosol, cytoplasm, and extracellular space (Fig. 4C). These findings confirm that fibrosis is a complex process in AM after invading the endometrial tissue into the myometrium.

Additionally, subcellular localization analysis revealed that many DEPs are in the extracellular regions (Fig. 5A). We further examined these DEPs located in the extracellular areas using MatrisomeDB 2.0, a database categorizing ECM matrisome proteins and ECM-related proteins[37,45]. Matrisome signatures of DEPs in ECM are presented in Fig. 5B. Adenomyotic myometrium contains a large number of collagens, such as collagen-4A1 (COL4A1), COL3A1, COL4A2, COL6A3, COL6A2, COL4A6, and COL1A2, whose excessive deposition lead to myometrial fibrosis. Additionally, fibronectin1 (FN1), secreted frizzled-related protein 4 (SFRP4), and laminin subunit beta-1 (LAMB1) are typical ECM proteins that promote fibroblast activation and ECM production (Fig. 5C). Furthermore, KEGG analysis revealed that the PI3K/AKT signaling pathway is one of the most significantly enriched pathways among ECM-associated DEPs (Fig. 5D).

Metabolomics analysis

The metabolomics sequencing process is illustrated in Fig. 6. Initially, data standardization for the identified metabolites demonstrated that the mean and quartile values were consistent across all metabolites, indicating good repeatability and accuracy(Fig. 6A). Sample repeatability testing followed, showing consistency in quantitative results from 10 biological replicates through a correlation heat map (Fig. 6B) and principal component analysis(Fig. 6C). Supplementary Fig. S2A–D confirmed the high accuracy and reliability of the mass spectrometry detection. Subsequently, metabolite content statistics were carried out using the KEGG

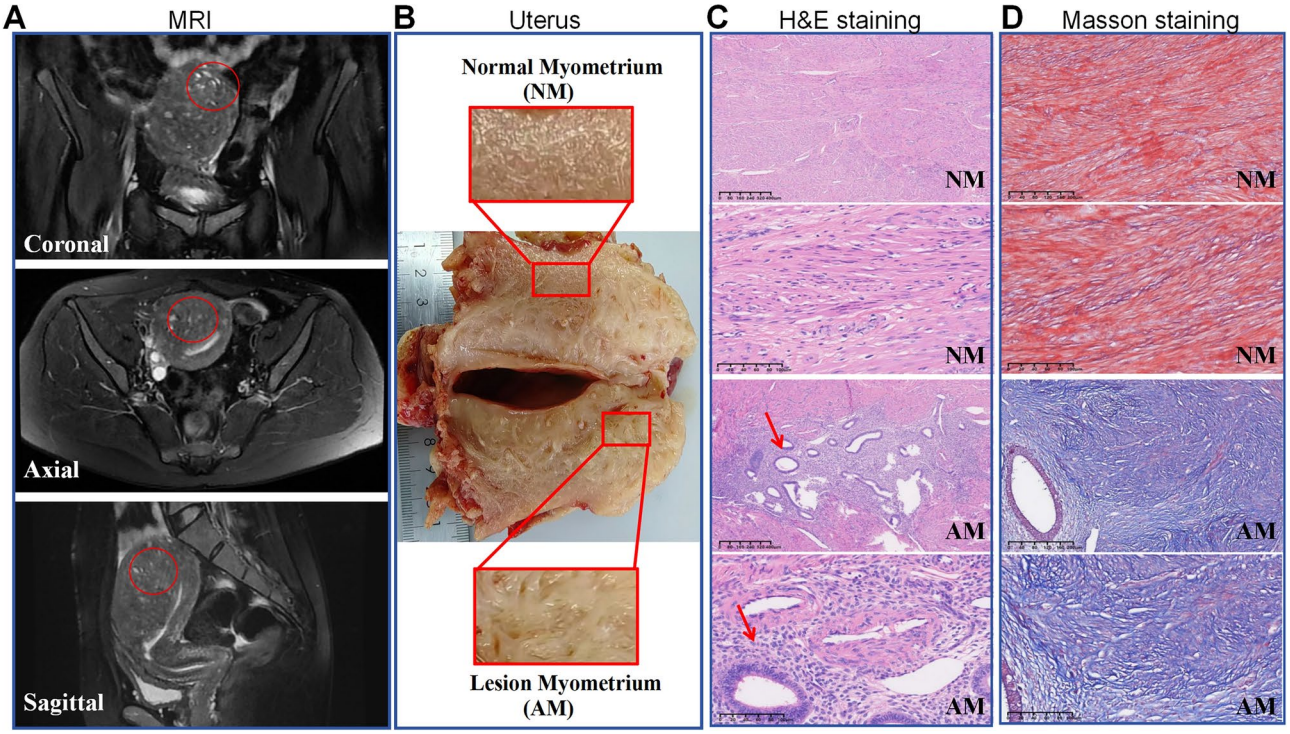

Fig. 2. Imaging and histological findings of AM. (**A**) Representative images of MRI for AM: The junctional zone is widened and blurred, the boundary between the deep and superficial muscle layers was unclear, the signal intensity was uneven, and scattered spot-like or round lipid-suppression hyperintense lesions are seen in the zone. From top to bottom are the Coronal, Axial, and Sagittal images. The circle indicates adenomyosis lesions. (**B**) Representative pictures of gross uterine specimen for AM. Above is the normal myometrium(NM) for control and the adenomyotic myometrium (AM) below. (**C**) Representative images of H&E staining in normal (top 2) and fibrotic adenomyotic myometrium (bottom 2). Arrows indicate endometrial glands and stroma. Scale bars, 400 μm and 100 μm, respectively. (**D**) Representative images of Masson trichrome staining in (top 2) and fibrotic adenomyotic myometrium (bottom 2). Scale bars, 200 μm and 100 μm, respectively.

database br08001 annotation, revealing significant metabolite composition differences between the AM and normal control groups (Figs. 6D and S2F). Cluster analysis was then employed to examine the similarity between samples and construct sample clusters. Figure 6E displayed variations among various samples or groups, whereas Fig. 6F depicted changes in metabolite expression levels within and across groups for different classifications of br08001.

To eliminate extraneous noise unrelated to metabolomic grouping, Partial Least Squares-Discriminant Analysis (OPLS-DA) was employed to validate group disparities. The OPLS-DA score plot, model validation, and S-plot revealed significant variation in metabolomic profiles between the AM and control groups, confirming the model's reliability and stability(Fig. 7A–C). Volcano plots (Fig. 7D) and cluster analysis heatmap(Fig. 7E) were constructed to display differences and significance in metabolite expression levels between the two sample groups; 37 metabolites were upregulated, and 79 were downregulated. Figure 7F displayed the top 20 metabolites with the two groups' most significant differential expression ratios. KEGG pathway enrichment results indicate that the DEMs are primarily enriched in caffeine metabolism, carbapenem biosynthesis, biosynthesis of alkaloids derived from histidine and purine, pantothenate and CoA biosynthesis, and metabolism of xenobiotics by cytochrome P450 (Fig. 7G). The differential metabolite classification diagram based on the HMDB Super class suggests that these metabolites mainly involve organoheterocyclic compounds, organic acids and derivatives, and lipids and lipid-like molecules (Fig. 7H).

Proteomics and metabolomics integrated analysis

In Fig. 8A, the DEMs and DEPs were mapped to the iPath platform, revealing intersections in key physiological processes like energy, carbohydrate, amino acid, nucleotide, and lipid metabolism. Correlation analysis presented as a heatmap (Fig. 8B) showed significant clustering of DEMs and DEPs. Proteins and metabolites with substantial correlations ($|r| \geq 0.6$) formed a co-expression network with 741 nodes and 14,085 edges (Fig. S3), indicating strong associations. Using the Metscape plugin in Cytoscape, a regulatory network of DEPs and DEMs was constructed to visualize compound networks, including structures, reaction types, enzymes, genes, and pathways. As shown in Fig. S4, at least 26 protein-metabolite modules were enriched, with enzymes or genes central and compounds peripheral. These analyses confirmed significant associations between protein and metabolite profiles in AM tissues, highlighting distinct functional modules.

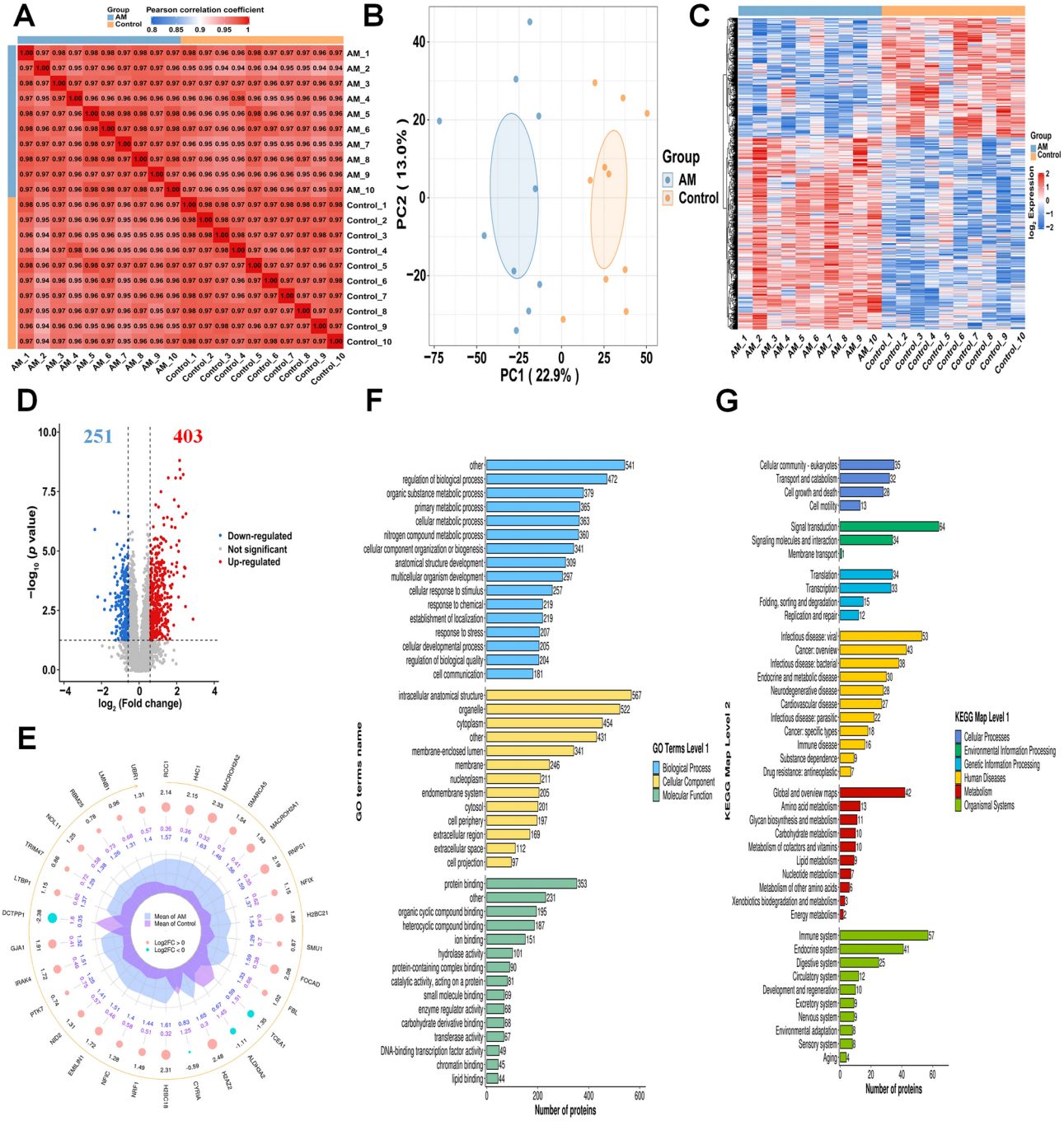

Fig. 3. Proteomic analysis of the myometrial tissue from normal myometrium(Control) and fibrotic adenomyotic myometrium (AM). (**A**) Heatmap of Pearson correlation coefficients between sample pairs. (**B**) Principal component analysis (PCA) of samples. (**C**) Hierarchical clustering heatmap of differential expression of proteins(DEPs). (**D**) Volcano plot of DEPs. (**E**) Radar chart depicting the top DEPs. (**F**) Gene Ontology (GO) analysis of DEPs. (**G**) Kyoto Encyclopedia of Genes and Genomes (KEGG) functional annotation classification of DEPs[36].

Given that the PI3K/AKT signaling pathway has been identified as a significantly enriched up-regulated pathway and is closely associated with fibrotic functions, we included the DEPs of the PI3K/AKT pathway and all DEMs in our integrative Spearman correlation analysis. The results showed that 10 metabolites are positively correlated with 11 proteins (CDKN1B, FN1, TNC, LAMB1, ITGA9, CREB1, CDC37, COL6A2, COL6A1, COL4A1, and TNXB), while 36 metabolites are negatively correlated (Fig. 8C). The correlation network diagram shows strong connections with a similarity score exceeding 0.7, comprising 57 nodes and 68 edges(Fig. 8D). LAMB1 has the most connections, followed by TNXB, TNC, and ITGA9. Additionally, the expression of fibrotic ECM proteins, such as FN1, TNC, ITGA9, COL4A1, and COL6A1, is abundant. These findings suggest a

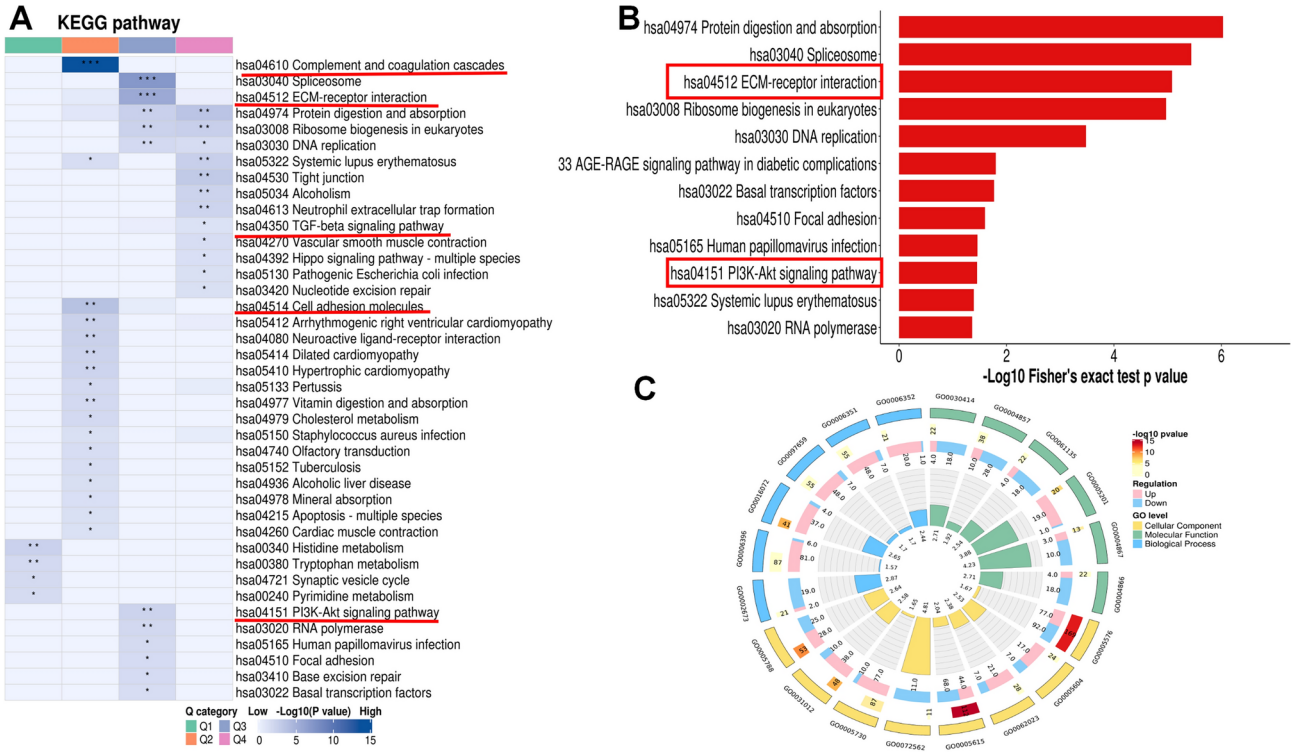

Fig. 4. Functional enrichment analysis of differentially expressed proteins. (**A**) Cluster analysis of KEGG pathway enrichment. Blue represents high enrichment significance, white represents low enrichment significance, * represents P value < 0.05, ** represents P value < 0.01, and *** represents P value < 0.001. (**B**) Bar graph of the significantly up-regulated KEGG pathway analysis. (**C**) Circos plot depicting GO enrichment analysis of DEPs.

significant association between metabolite regulation and the PI3K/AKT signaling pathway in the fibrosis of the adenomyotic myometrium.

Verification of DEPs and PI3K/AKT signaling pathways in fibrotic adenomyotic myometrium

To validate the DEPs and key signaling pathways proteins identified through proteomic profiling, we conducted a western blotting assay on uterine tissue from 6 additional AM patients who underwent hysterectomy. As illustrated in Fig. 9A and B, the western blot analyses revealed that serine-threonine Kinase 11 (STK11), also known as liver kinase B1 (LKB1), SFRP4, high mobility group protein3 (HMGB3), FN1, Collagen IV, and myosin heavy chain9 (MYH9) were significantly upregulated in the adenomyotic myometrium, consistent with the proteomic results. Notably, the increased deposition of SFRP4, FN1, and Collagen IV suggests the presence of myometrial fibrosis. Furthermore, the expression levels of phosphorylated PI3K (p-PI3K) and p-AKT proteins were significantly elevated in the AM group, accompanied by similar changes in the p-AKT/AKT and p-PI3K/PI3K ratios. These findings suggest that the PI3K/AKT signaling pathway is activated in adenomyotic myometrium fibrosis, indicating the existence of a pro-inflammatory, profibrotic, and anti-angiogenic microenvironment in the fibrotic myometrium associated with AM.

Analyzing α-SMA expression correlation with DEPs in fibrotic adenomyotic myometrium

To explore the transformation of stromal cells into myofibroblasts within the adenomyotic myometrium, we assessed the expression of specific marker proteins in adenomyotic lesions of patients who underwent hysterectomy, utilizing immunohistochemical staining techniques. As illustrated in Fig. 10A, CD10 showed strong positivity within the adenomyotic lesions, indicating the presence of endometrial stromal cells. In the same CD10-positive regions, α-SMA protein was abundantly expressed, whereas caldesmon expression was undetectable, confirming the metaplasia of stromal cells into myofibroblasts. The classical fibrosis marker of FN1 was also significantly higher expression in this adenomyotic region, suggesting fibrosis formation. Furthermore, p-AKT exhibited strong positivity within stromal cells featuring myofibroblasts, with significantly higher expression levels than those smooth muscle cells of the normal myometrium. Conversely, AKT expression intensity was approximately equivalent in adenomyotic and normal myometrial tissues. These findings highlight a strong correlation between AKT phosphorylation and AM-associated fibrosis, underscoring the critical role of the PI3K/AKT signaling pathway in the pathogenesis of AM (Fig. 10B).

To further elucidate the relevance of stromal cell metaplasia into myofibroblasts in myometrial fibrosis, we conducted a correlation analysis between α-SMA expression scores and the ratios of ECM-associated DEPs in AM patients who underwent multi-omics studies, as previously described. Predictably, the expression ratio

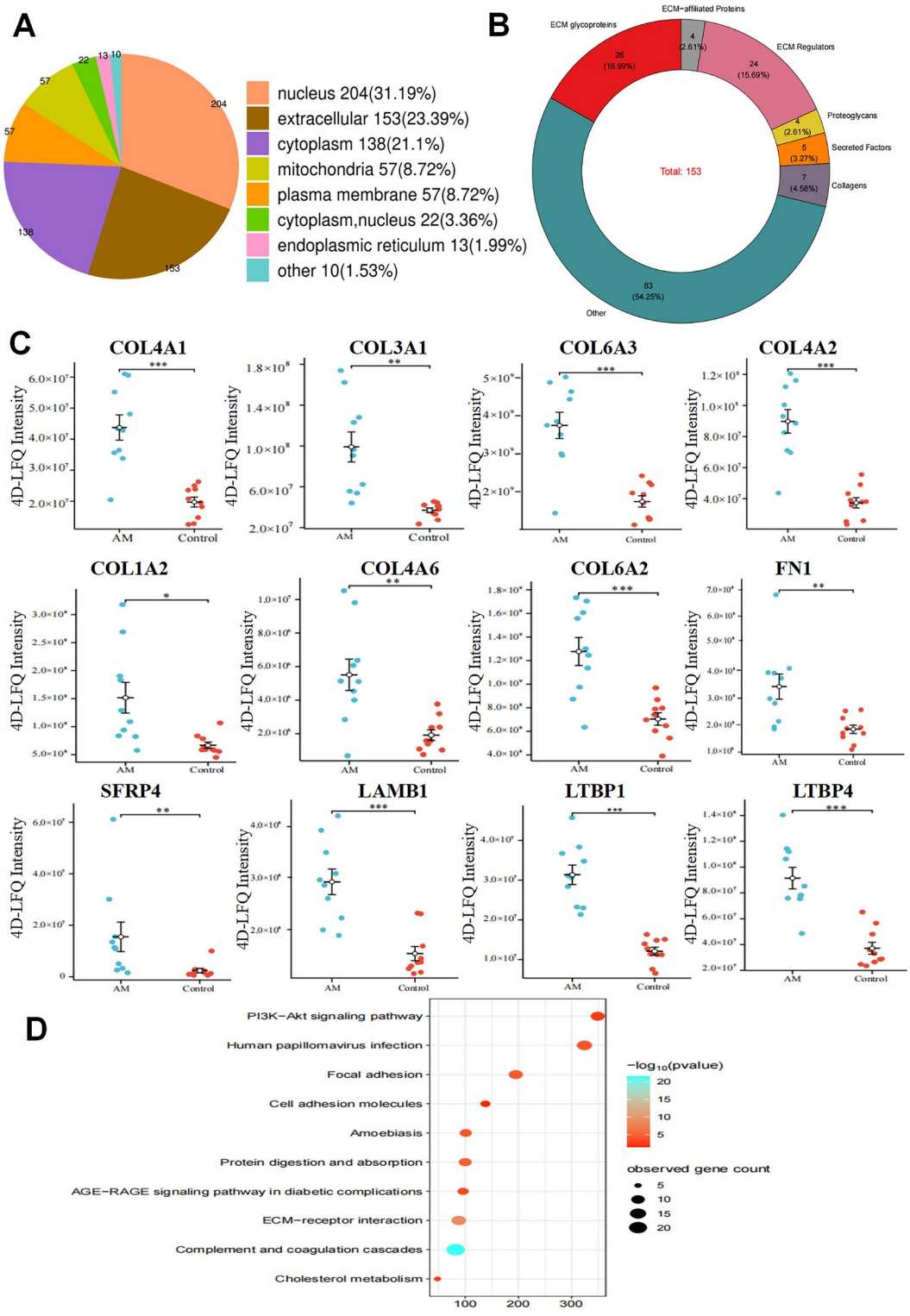

Fig. 5. Quantitative analysis of the extracellular matrix (ECM) proteins between normal myometrium (Control) and fibrotic adenomyotic myometrium(AM). (**A**) Subcellular localization of DEPs. (**B**) The pie chart shows the numbers of each category of all quantified differential ECM proteins. (**C**) The 4D label-free quantified (LFQ) expression of partial ECM proteins in normal myometrium(Control) and fibrotic adenomyotic myometrium (AM) (n = 10 independent samples, *P < 0.05 and **P < 0.01). (**D**) Bubble plot of KEGG pathway enrichment analysis of ECM protein network.

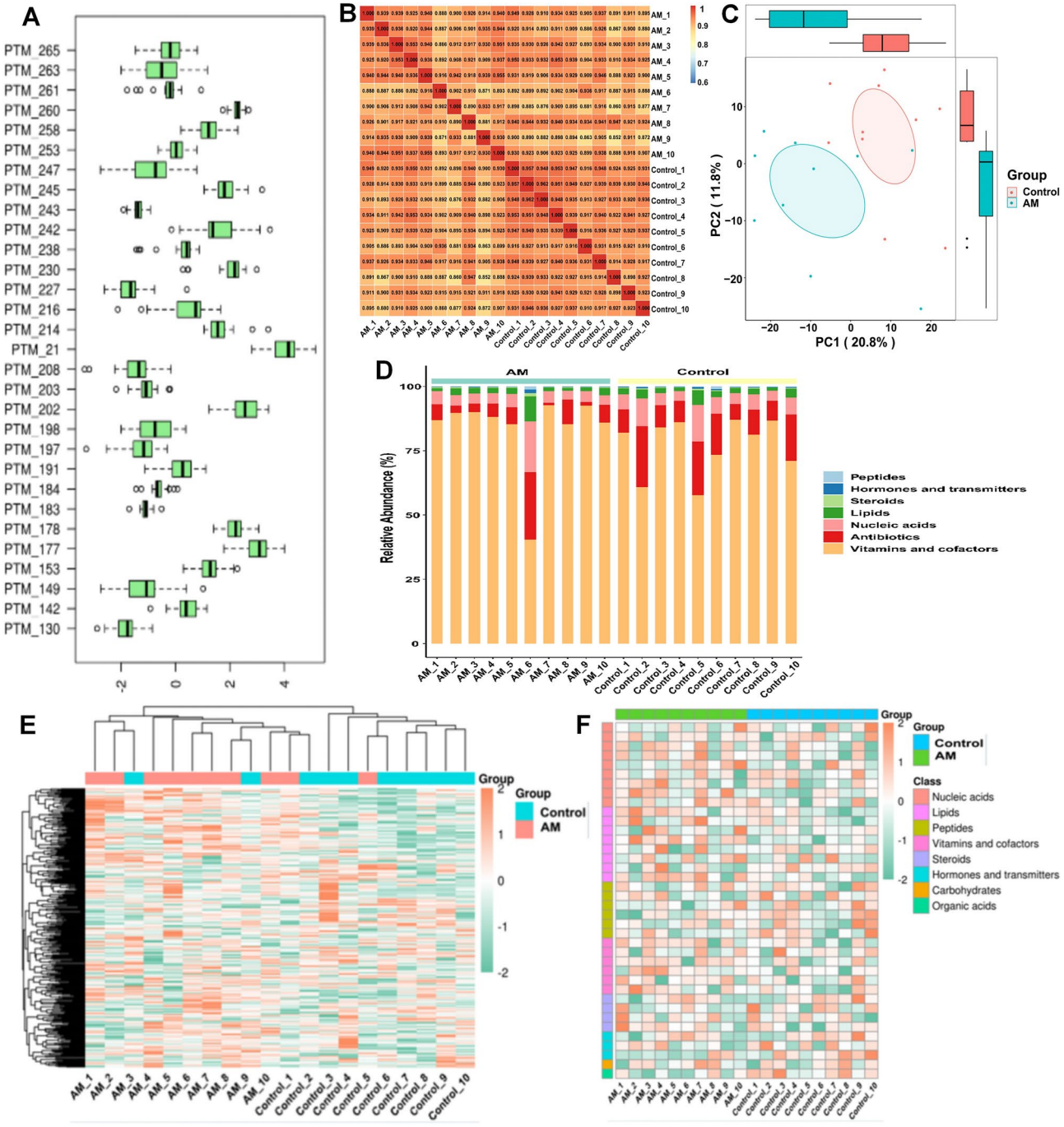

Fig. 6. Metabolomic analysis of the myometrial tissue from normal myometrium(Control) and fibrotic adenomyotic myometrium(AM). (**A**) Forest plot of metabolite standardization. (**B**) Heatmap depicting the Pearson correlation coefficients between pairs of samples. (**C**) Principal component analysis of sample data. (**D**) Percentage stacked bar chart of metabolite content statistics. (**E**) Heatmap of inter-group clustering of metabolites. (**F**) Heatmap of KEGG database br08001 classification.

of fibrosis-related proteins (COL1A2, COL3A1, COL4A2, COL6A2, COL6A3, FN1, LTBP1, and LTBP4) in adenomyotic lesions correlated positively with α-SMA expression score(all p-value < 0.05, R > 0.6) (Fig. 10C). These findings indicate that AM's adenomyotic myometrium fibrogenesis is significantly associated with stromal cell metaplasia into myofibroblasts.

Behaviors of the myofibroblasts as regulated by PI3K/AKT singing pathway invitro

We initially conducted primary culture and characterization of myofibroblasts to validate the findings from multi-omics, western blotting assays, and immunohistochemistry (IHC). Under light microscopy, the cells appeared large and polygonal with multiple extended processes (Fig. 11A). IF assay showed negative caldesmon staining,

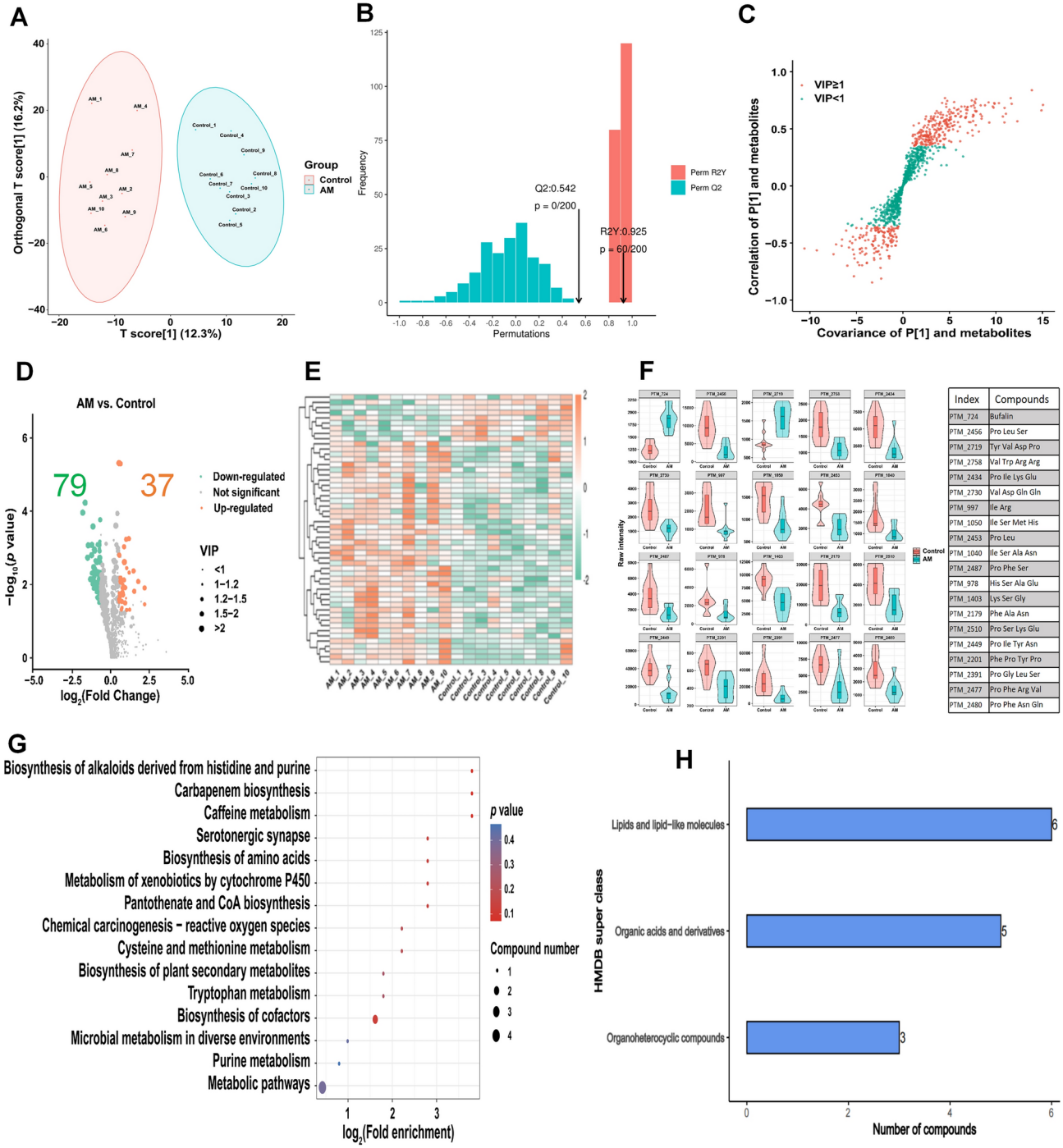

Fig. 7. Partial Least Squares-Discriminant (OPLS-DA) and differentially expressed metabolites (DEMs) analysis between the AM and control group. (**A**) Metabolite OPLS-DA score plot. (**B**) Model validation plot of metabolite OPLS-DA. (**C**) Metabolite OPLS-DA S-plot. (**D**) Volcano plot of differentially expressed metabolites. (**E**) Heatmap of clustered differentially expressed metabolites. (**F**) Violin plot comparing important differentially expressed metabolites between groups. (**G**) KEGG enrichment analysis of differentially expressed metabolites. (**H**) Annotation and classification of differentially expressed metabolites in HMDB.

slight positivity for CD10, and strong positivity for α-SMA (Fig. 11B). These results indicate the successful extraction of myofibroblasts from adenomyotic myometrium. Subsequently, we treated these myofibroblasts with the dual PI3K/AKT inhibitor(PI3K/AKT-IN-1). Figure 11C and D illustrate the results of the EdU assay, which indicated a significant decrease in cell proliferation, as demonstrated by both green fluorescence staining and the percentage of positive cells ($p = 0.031$). Similarly, Western blot analysis revealed statistically significant reductions in the expression levels of FN1, Collagen IV, p-AKT, and p-PI3K in the inhibitor-treated group, as

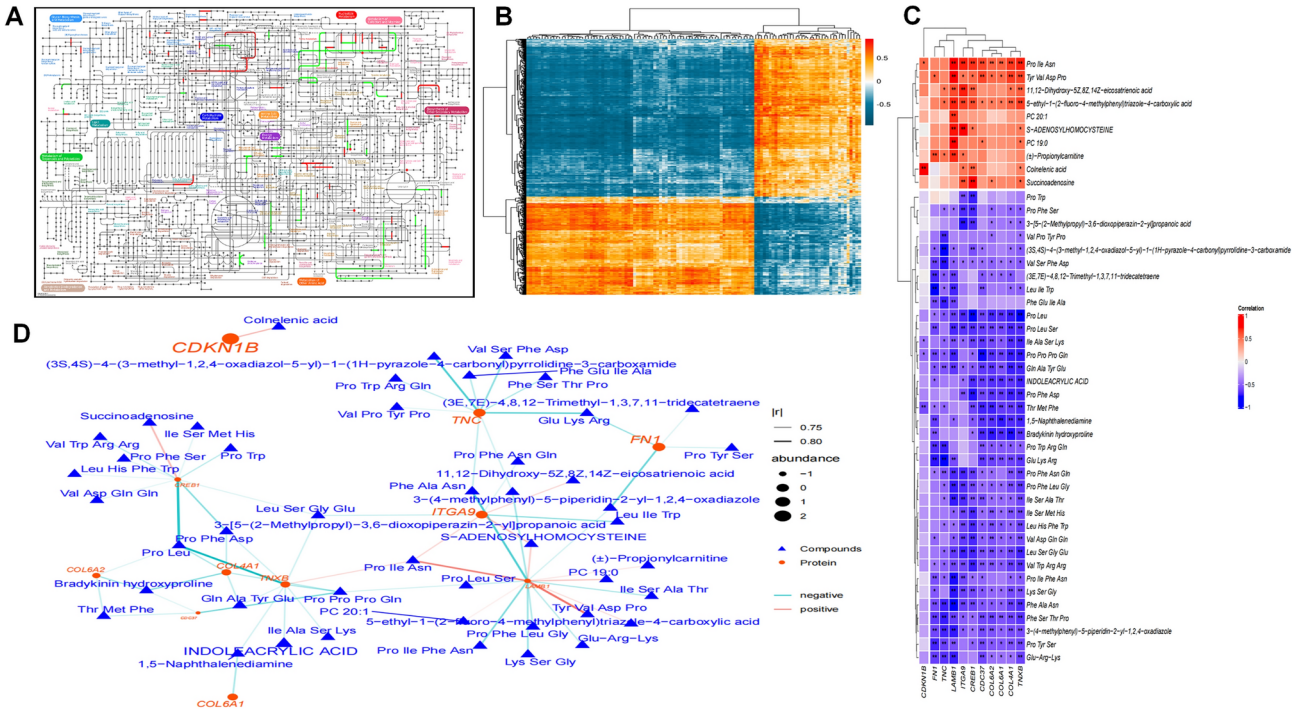

Fig. 8. Pathway analysis of integrated differentially expressed proteins and metabolites in adenomyosis. (**A**) IPath pathway analysis of the differentially expressed metabolites and proteins. (**B**) Heatmap illustrating the quantitative correlation coefficients between proteomics and metabolomics. (**C**) Heatmap analysis was performed using Spearman correlation analysis, showing the relation between PI3K/AKT pathway protein and DEMs. The color key indicates correlation strengths,* represents P value < 0.05, ** represents P value < 0.01. (**D**) Relevance network graph depicting correlations derived from Spearman correlation analysis between PI3K/AKT pathway and DEMs.

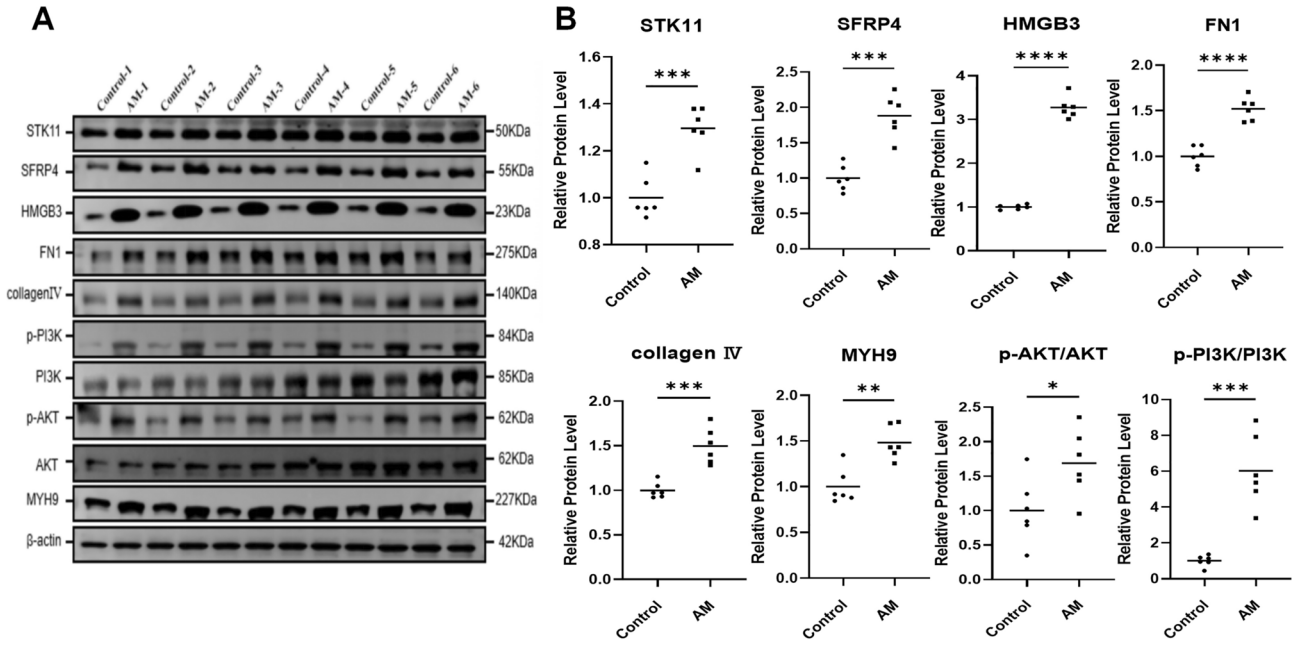

Fig. 9. Verification of differential protein expression and key proteins of signaling pathways in fibrotic adenomyotic myometrium. Representative Western blot analyses of STK11, SFRP4, HMGB3, FN1, Collagen IV, AKT, p-AKT, PI3K, p-PI3K, and MYH9 (**A**) and quantitative data including p-AKT/AKT and p-PI3K/PI3K (**B**) are shown (n = 6 independent samples, * represents P value < 0.05, ** represents P value < 0.01, *** represents P value < 0.001,****represents P value < 0.0001, and ns).

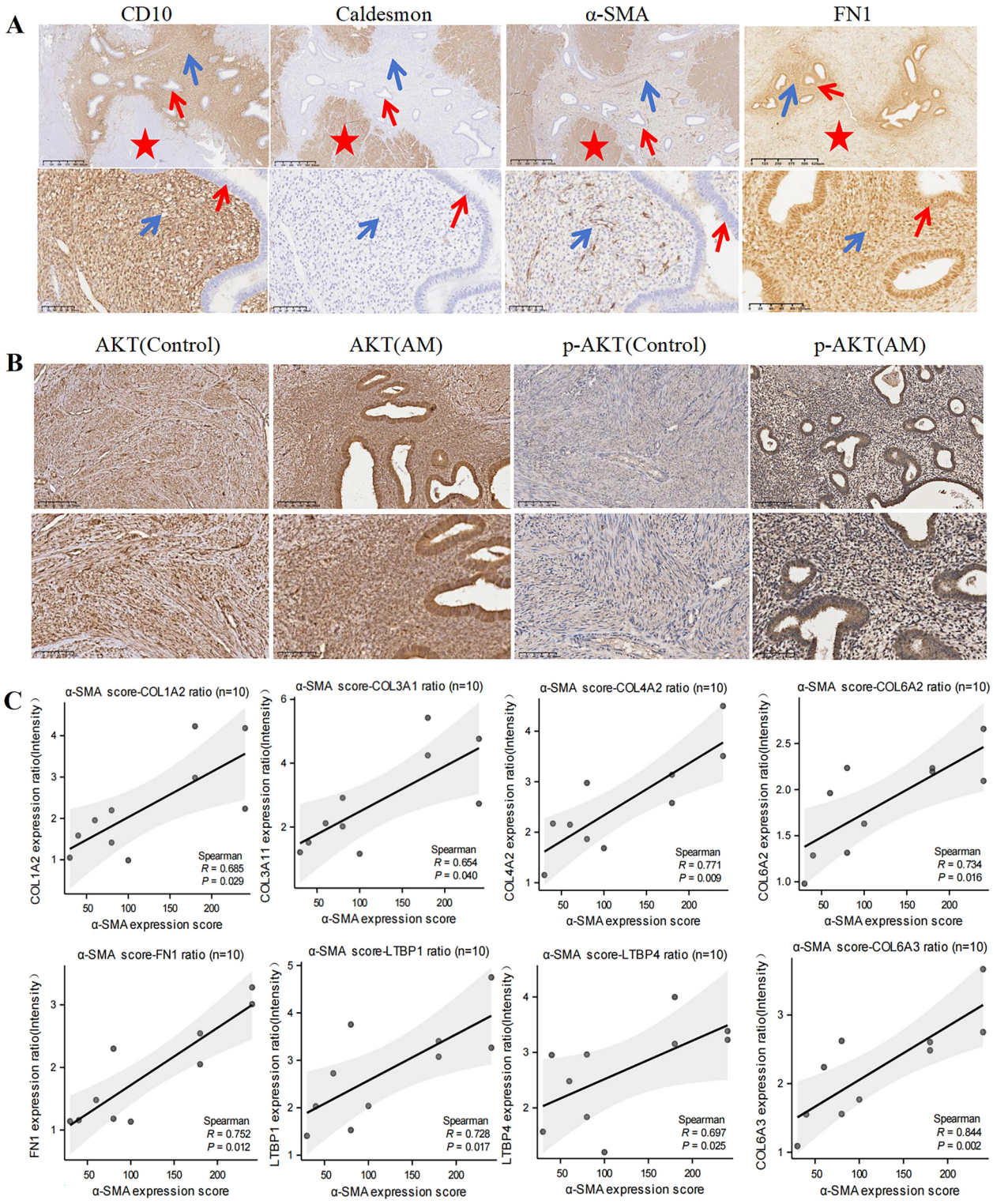

Fig. 10. Immunohistochemical(IHC) analysis for stromal cell metaplasia and the correlation between its α-SMA expression and DEPs ratio in adenomyosis. (**A**) Representative micrographs show the expression and localization of CD10, Caldesmon, α-SMA, and FN1 in the interstitial cells of adenomyotic tissue from patients. The red arrows indicate epithelial cells, while the blue ones indicate stromal cells. The red Star indicates the smooth muscle cells at the periphery of the stromal cells. Scale bars: 625 μm (up) and 100 μm (bottom), respectively. (**B**) Representative micrographs show the expression and localization of AKT and p-AKT in adenomyotic myometrium and normal myometrial tissue. Scale bars: 200 μm (up) and 100 μm (bottom), respectively. (**C**) Scatter plot of the extent of COL1A2, COL3A1, COL4A2, COL6A2, FN1, LTBP1, and LTBP4 expression difference ratio in fibrotic adenomyotic myometrium versus the α-SMA expression score in the myofibroblasts.

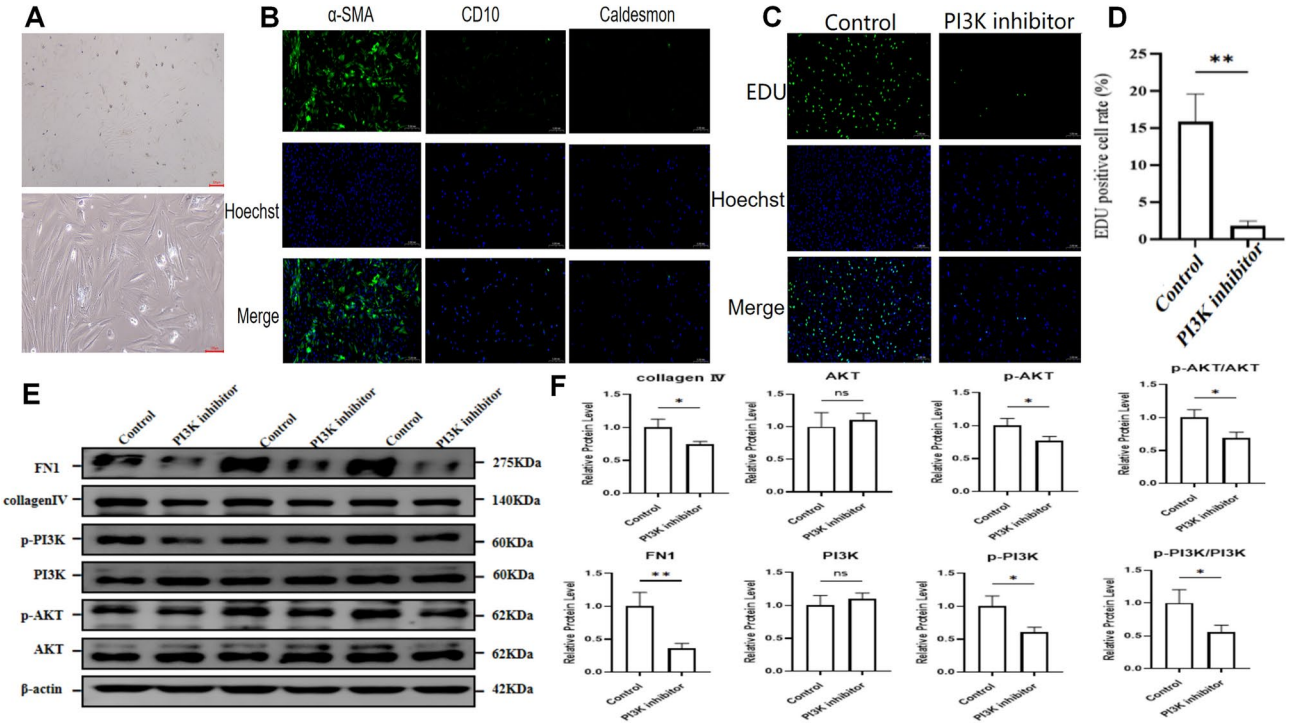

Fig. 11. Cell culture, WB, and IF method verification for key targets in signaling pathways. (**A**) Cells primary culture. Representative micrographs show myofibroblasts morphology. Scale bar: 100 μM (up) and 200 μM(bottom). (**B**) Immunofluorescence staining shows the fluorescent expression of α-SMA, CD10, and caldesmon (Scale bar: 100 μM). (**C**,**D**) EdU assay. Representative IF staining of EDU assay (**E**) and quantitative data (**D**) are shown (Scale bar:200 μM, n = 3). (**E**,**F**) Western blot analyses show different groups' FN1, COL4, PI3K, AKT, p-PI3K, and p-PAKT protein expression. Representative Western blot (**E**) and quantitative data (**F**) are shown(n = 3 independent samples, * represents *P* value < 0.05, ** represents *P* value < 0.01 and ns).

detailed in Fig. 11E and F. A corresponding decrease in the ratios of p-PI3K/PI3K and p-AKT/AKT was also observed (all $p < 0.05$, Fig. 11F).

Discussion

AM is known to be characterized by endometrial glands and stromal components within the myometrium. These ectopic endometrium undergo periodic bleeding, leading to recurrent damage and repair of the myometrial tissue[46]. It is well established that repeated tissue injury and abnormal repair cause fibrosis[47], likely leading to the formation and progression of fibrosis in AM[8]. Therefore, this fibrogenic microenvironment's molecular composition and underlying mechanisms must be fully characterized. In this study, we employed a four-dimensional platform combined with an LC–MS/MS approach to unravel the proteomic and metabolomic landscape, revealing proteome-wide and metabolite-wide alterations in normal and fibrotic myometrium of AM. Integrative analysis indicated that the significantly enriched up-regulated PI3K/AKT pathway was closely correlated with DEMs in the fibrotic myometrium of AM. Furthermore, we demonstrated experimentally the omics findings that the activation of the PI3K/AKT signaling pathway is related to fibrosis in AM's myometrium. These findings provide the first comprehensive proteomic and metabolomic characterization of fibrotic myometrium in AM, offering important insights into the molecular composition and potential mechanisms of the fibrotic microenvironment.

Clinical manifestations of AM show considerable individual heterogeneity, with significant differences in age, dysmenorrhea, menorrhagia, and infertility observed among different AM subtypes[48]. This variability is believed to be related to the self-repair response of myometrial tissue following endometrial invasion, involving continuous reactions including sex hormone imbalances, neuroangiogenesis, inflammation, fibrosis, and cell proliferation[49]. Therefore, elucidating the pathogenesis of AM through mechanistic responses following the invasion of endometrial components into the myometrium provides an opportunity to develop targeted therapies. Accordingly, the present study focused on the molecular mechanisms underlying the cascade initiated after this invasion of endometrial stroma and glands, drawing upon research comparing normal myometrium with that affected by adenomyosis. This approach contrasts with previous studies that examined damage at the endometrial-myometrial interface, increased invasiveness of endometrial tissue, and myometrial stem cell metaplasia[50]. Building on this perspective, we suggest that future research should involve three distinct study groups: (1) control myometrium from healthy patients, (2) myometrium from adenomyosis patients without visible lesions, and (3) adenomyotic lesions. This would enhance understanding of disease development and early

molecular changes. By highlighting this approach, our study seeks to contribute to the secondary prevention of AM and provide insights into its pathogenesis, paving the way for effective therapies.

In proteomics related to AM myometrial fibrosis, prominent DEPs include CHDH, H2AZ2, SFRP4, CENPV, and HMGB3, etc. Many of these proteins are reported here for the first time. SFRP4, a profibrotic signature of fibroblast[51], is closely linked to dysmenorrhea symptoms via the COX-2 pathway[12]. Some studies suggest that SFRP4 + IGFBP5hiNKT cells can transform stem cells into neurogenic cells, thus inducing AM pain[52]. Additionally, a single-cell transcriptomic analysis reveals differential high expression of SFRP4 involving the WNT signaling pathway in adenomyotic fibroblasts, contributing a crucial role in the pathophysiology of AM[53]. Furthermore, KEGG analysis highlighted the three most significant enrichment pathways, all demonstrating a strong association with the regulation of fibrosis. For example, complement and coagulation cascades interact with the immune system and are key modulators of extracellular matrix deposition, leading to scarring and fibrosis[54]. An imbalance in ECM regulation can result in cell-ECM-cell crosstalk, contributing to fibrosis progression[55]. Targeted inhibition of ECM-receptor interaction is a primary strategy against fibrosis[56]. The PI3K/AKT signaling pathway is crucial in fibrosis[29].

Moreover, further subcellular localization analysis revealed that most of these DEPs are situated in the extracellular regions, containing a large number of fibrosis-related proteins, such as FN1, collagen (COL1A2, COL4A1, and COL6A3, etc.), TGF-β-binding protein 1 (LTBP1), and LTBP4. The results of the KEGG enrichment analysis revealed that these DEPs were significantly enriched in pathways such as the PI3K-Akt signaling pathway, complement and coagulation cascades, ECM-receptor interaction, cell adhesion molecules, etc. Recent studies have demonstrated that the high abundance of LTBP1 is crucial in regulating smooth muscle regeneration and differentiation[37,57]; anti-LTBP4 antibody has been shown to improve muscle function and reduce muscle fibrosis in muscular dystrophy[58], highlighting its potential role in fibrosis development. These findings indicate that these DEPs may play a significant role in promoting the formation of AM-related fibrosis. We further examined ECM-specific proteins using a database that categorizes ECM matrisome proteins, highlighting the role of ECM-associated proteins in myometrial fibrogenesis. These findings may serve as a core set of signature proteins for AM fibrosis, and they propose that these proteins contribute to establishing the fibrotic microenvironment.

There remains a paucity of studies employing metabolomics techniques to investigate the metabolic alterations associated with AM[59]. The inaugural untargeted serum metabolomics study on AM revealed that patients exhibited lower concentrations of 3-hydroxybutyrate, glutamate, and serine, and higher concentrations of proline, choline, citrate, 2-hydroxybutyrate, and creatinine[21]. Furthermore, another metabolomics study on myometrial specimens from AM patients suggests that inflammation, oxidative stress, cell proliferation and apoptosis, and energy metabolism may play roles in the progression of AM[20]. In our current study, DEMs mainly involve processes such as caffeine metabolism, carbapenem biosynthesis, biosynthesis of alkaloids derived from histidine and purine, pantothenate and A biosynthesis, and the metabolism of xenobiotics by cytochrome P450. Although many differential metabolites and biological processes are underreported and lack a unified conclusion, these findings provide insights into the metabolic changes associated with AM fibrosis, potentially contributing to understanding the disease's pathogenesis and molecular mechanisms. Furthermore, Our quantitative correlation and interaction network analyses have revealed significant associations between DEPs and DEMs in AM fibrosis tissues. These analyses have identified distinct functional modules, underscoring this condition's dynamic regulation and complex interactions between proteins and metabolites. Notably, the significant correlation between DEPs associated with the PI3K/AKT signaling pathway and DEMs underscores the dominant role of this pathway in regulating fibrosis in AM.

Although the underlying molecular mechanisms that lead to the development of fibrosis are complex, the PI3K/AKT signaling pathway is a key regulator in fibrogenesis and is under investigation as a therapeutic target for some fibrotic diseases[29–32]. Unlike previous studies that emphasized the role of the PI3K/AKT pathway in promoting uterine smooth muscle cell proliferation and epithelial proliferation in AM[26,27], our multi-omics data, supported by clinical validation, demonstrate significant upregulation of the PI3K/AKT signaling pathway specifically in fibrotic myometrium lesions. Correlation analysis further confirmed that the differential expression of fibrosis-related proteins is positively correlated with the expression of α-SMA in myofibroblasts within AM lesions. In vitro experiments showed that a PI3K/AKT inhibitor can alleviate myometrial fibrosis. These findings suggest that myometrial fibrosis in AM is associated with myofibroblast activation and involves dysregulated PI3K/AKT-driven mechanisms, expanding its implications beyond cellular proliferation and offering novel insights into the pathogenesis of AM. This underscores antifibrotic treatment as a promising therapy. Nonetheless, the fibrosis mechanisms in AM are complex and may involve multiple pathways, warranting further in-depth investigation.

This study presents several advantages over previous research. It is the first to integrate proteomic and metabolomic analyses of AM lesions. Utilizing standardized tissue samples and analytical platforms reduced analysis bias. The study comprehensively elucidates AM proteomics through expression profiling and biological function analysis and provides a detailed AM metabolic map, revealing pathological pathways and potential treatment targets. Additionally, in vitro experiments were conducted to establish a foundation for investigating the molecular mechanisms of myometrial fibrosis in adenomyosis. However, limitations remain, such as further exploring the clinical applicability of differentially expressed proteins and metabolites. Confounding factors could affect the omics data, especially metabolomics, which is prone to noise. This preliminary study requires validation with larger clinical samples and animal studies. Despite identifying significant molecular changes in fibrogenic myometrial protein and metabolic profiles, pinpointing key regulators is challenging and necessitates further research for clinical validation.

Conclusion

Fibrosis in the myometrium of AM lesions demonstrates distinct proteomic and metabolomic expression profiles. Integrated analysis has confirmed significant associations between the protein and metabolite profiles in AM tissues, with the PI3K/AKT pathway playing an important regulatory role. Subsequent experiments support these multi-omics findings, highlighting the crucial involvement of the PI3K/AKT signaling pathway in AM fibrosis. Therefore, comparative proteomic and metabolomic analyses are invaluable for elucidating the pathological mechanisms underlying myometrial fibrosis in AM and suggest that antifibrotic treatment could be a promising therapeutic strategy. However, the mechanisms of AM fibrosis are complex, and further investigation is required to fully understand the targeted regulatory pathways involved.

Data availability

The main data generated or analyzed during this study are included in this manuscript and its Additional files and are available from the corresponding author on reasonable request. The mass spectrometry proteomics data have been deposited to the ProteomeXchange Consortium via the PRIDE partner repository with the dataset identifier PXD058989. Metabolomics data have been deposited to the EMBL-EBI MetaboLights database with the identifier MTBLS11965.

Received: 20 December 2024; Accepted: 10 April 2025
Published online: 20 April 2025

References

1. Chapron, C. et al. Diagnosing adenomyosis: An integrated clinical and imaging approach. *Hum. Reprod. Update* **26**(3), 392–411 (2020).
2. Kho, K. A., Chen, J. S. & Halvorson, L. M. Diagnosis, evaluation, and treatment of adenomyosis. *JAMA* **326**(2), 177–178 (2021).
3. Wu, H. M. et al. The current understanding of molecular mechanisms in adenomyosis-associated infertility and the treatment strategy for assisted reproductive technology. *Int. J. Mol. Sci.* **25**(16), 8937 (2024).
4. Upson, K. & Missmer, S. A. Epidemiology of adenomyosis. *Semin. Reprod. Med.* **38**(2–03), 89–107 (2020).
5. Osada, H. Uterine adenomyosis and adenomyoma: the surgical approach. *Fertil. Steril.* **109**(3), 406–417 (2018).
6. Schrager, S. et al. Adenomyosis: Diagnosis and management. *Am. Fam. Phys.* **105**(1), 33–38 (2022).
7. Bulun, S. E. et al. Adenomyosis pathogenesis: Insights from next-generation sequencing. *Hum. Reprod. Update* **27**(6), 1086–1097 (2021).
8. Liu, X. et al. Corroborating evidence for platelet-induced epithelial-mesenchymal transition and fibroblast-to-myofibroblast transdifferentiation in the development of adenomyosis. *Hum. Reprod.* **31**(4), 734–749 (2016).
9. Guo, S. W. Cracking the enigma of adenomyosis: An update on its pathogenesis and pathophysiology. *Reproduction* **164**(5), R101–R121 (2022).
10. Rutledge, J., Oh, H. & Wyss-Coray, T. Measuring biological age using omics data. *Nat. Rev. Genet.* **23**(12), 715–727 (2022).
11. Babu, M. & Snyder, M. Multi-omics profiling for health. *Mol. Cell Proteomics* **22**(6), 100561 (2023).
12. Zhang, J. et al. Proteomic detection of COX-2 pathway-related factors in patients with adenomyosis. *PeerJ* **12**, e16784 (2024).
13. Chen, D. et al. Comparative proteomics identify HSP90A, STIP1 and TAGLN-2 in serum extracellular vesicles as potential circulating biomarkers for human adenomyosis. *Exp. Ther. Med.* **23**(6), 374 (2022).
14. Liu, F. et al. Endometrial stromal cell proteomic analysis reveals LIM and SH3 protein 1 (LASP1) plays important roles in the progression of adenomyosis. *Mol. Hum. Reprod.* https://doi.org/10.1093/molehr/gaab008 (2021).
15. Xiaoyu, L. et al. Serum differential proteomic analysis of endometriosis and adenomyosis by iTRAQ technique. *Eur. J. Obstet. Gynecol. Reprod. Biol.* **182**, 62–65 (2014).
16. Xiaoyu, L. et al. Comparative serum proteomic analysis of adenomyosis using the isobaric tags for relative and absolute quantitation technique. *Fertil. Steril.* **100**(2), 505–510 (2013).
17. Long, X. et al. Evaluation of novel serum biomarkers and the proteomic differences of endometriosis and adenomyosis using MALDI-TOF-MS. *Arch. Gynecol. Obstet.* **288**(1), 201–205 (2013).
18. Zhou, S. et al. Proteomics identification of annexin A2 as a key mediator in the metastasis and proangiogenesis of endometrial cells in human adenomyosis. *Mol. Cell Proteomics* **11**(7), M112 017988 (2012).
19. Bourdon, M. et al. Adenomyosis is associated with specific proton nuclear magnetic resonance ((1)H-NMR) serum metabolic profiles. *Fertil. Steril.* **116**(1), 243–254 (2021).
20. Song, W. et al. Integrative metabolomic profiling reveals aberrations in myometrium associated with adenomyosis: a pilot study. *Reprod. Biol. Endocrinol.* **20**(1), 49 (2022).
21. Chen, P. et al. An insight into gut microbiota and metabolites in the mice with adenomyosis. *Front. Cell Infect. Microbiol.* **13**, 1075387 (2023).
22. Ristori, M. V. et al. Proteomics and metabolomics approaches towards a functional insight onto AUTISM spectrum disorders: Phenotype stratification and biomarker discovery. *Int. J. Mol. Sci.* **21**(17), 6274 (2020).
23. Dubin, R. F. & Rhee, E. P. Proteomics and metabolomics in kidney disease, including insights into etiology, treatment, and prevention. *Clin. J. Am. Soc. Nephrol.* **15**(3), 404–411 (2020).
24. Huang, X. et al. Integrated multi-omics analysis to reveal the molecular mechanisms of inflorescence elongation in medicago sativa. *Int. J. Mol. Sci.* **25**(12), 6497 (2024).
25. Chan, K. T. et al. A functional genetic screen defines the AKT-induced senescence signaling network. *Cell Death Differ.* **27**(2), 725–741 (2020).
26. Sirohi, V. K. et al. Regulation of AKT signaling in mouse uterus. *Endocrinology* https://doi.org/10.1210/endocr/bqab233 (2022).
27. Streuli, I. et al. Activation of the MAPK/ERK cell-signaling pathway in uterine smooth muscle cells of women with adenomyosis. *Reprod. Sci.* **22**(12), 1549–1560 (2015).
28. Zhang, K. et al. Mechanism study of *Cinnamomi ramulus* and *Paris polyphylla* Sm. drug pair in the treatment of adenomyosis by network pharmacology and experimental validation. *Evid. Based Complement. Alternat. Med.* **2022**, 2624434 (2022).
29. Wang, J. et al. Targeting PI3K/AKT signaling for treatment of idiopathic pulmonary fibrosis. *Acta Pharm. Sin. B* **12**(1), 18–32 (2022).
30. Deng, L. et al. Icariside II modulates pulmonary fibrosis via PI3K/Akt/beta-catenin pathway inhibition of M2 macrophage program. *Phytomedicine* **130**, 155687 (2024).
31. Zhang, S. et al. Metabolomics reveals that chronic restraint stress alleviates carbon tetrachloride-induced hepatic fibrosis through the INSR/PI3K/AKT/AMPK pathway. *J. Mol. Med.* **102**(1), 113–128 (2024).
32. Li, R. et al. Fufang Shenhua tablet inhibits renal fibrosis by inhibiting PI3K/AKT. *Phytomedicine* **116**, 154873 (2023).

33. Gao, H. et al. Uterine size and volume are associated with a higher clinical pregnancy rate in patients undergoing assisted reproduction technology: A longitudinal study (A STROBE-compliant article). *Medicine* **98**(8), e14366 (2019).
34. Cox, J. & Mann, M. MaxQuant enables high peptide identification rates, individualized p.p.b.-range mass accuracies and proteome-wide protein quantification. *Nat. Biotechnol.* **26**(12), 1367–1372 (2008).
35. Cantalapiedra, C. P. et al. eggNOG-mapper v2: Functional annotation, orthology assignments, and domain prediction at the metagenomic scale. *Mol. Biol. Evol.* **38**(12), 5825–5829 (2021).
36. Kanehisa, M. et al. KEGG for taxonomy-based analysis of pathways and genomes. *Nucleic Acids Res.* **51**(D1), D587-d592 (2023).
37. Zhao, L. M. et al. Promotion of uterine reconstruction by a tissue-engineered uterus with biomimetic structure and extracellular matrix microenvironment. *Sci. Adv.* **9**(46), eadi6488 (2023).
38. Ashburner, M. et al. Gene ontology: Tool for the unification of biology. The Gene Ontology Consortium. *Nat. Genet.* **25**(1), 25–29 (2000).
39. Ogata, H. et al. KEGG: Kyoto encyclopedia of genes and genomes. *Nucleic Acids Res.* **27**(1), 29–34 (1999).
40. Chan, B. High-level quantum chemistry reference heats of formation for a large set of C, H, N, and O species in the NIST chemistry webbook and the identification and validation of reliable protocols for their rapid computation. *J. Phys. Chem. A* **126**(30), 4981–4990 (2022).
41. Wishart, D. S. et al. HMDB 5.0: The Human Metabolome Database for 2022. *Nucleic Acids Res.* **50**(D1), D622–D631 (2022).
42. Gao, J. et al. Metscape: A cytoscape plug-in for visualizing and interpreting metabolomic data in the context of human metabolic networks. *Bioinformatics* **26**(7), 971–973 (2010).
43. Madrid-Gambin, F. et al. Integrated lipidomics and proteomics point to early blood-based changes in childhood preceding later development of psychotic experiences: Evidence from the avon longitudinal study of parents and children. *Biol. Psychiatry* **86**(1), 25–34 (2019).
44. Zhang, Y. et al. Nuclear translocation of cleaved PCDH9 impairs gastric cancer metastasis by downregulating CDH2 expression. *iScience* **27**(2), 109011 (2024).
45. Schneider, K. H. et al. Acellular vascular matrix grafts from human placenta chorion: Impact of ECM preservation on graft characteristics, protein composition and in vivo performance. *Biomaterials* **177**, 14–26 (2018).
46. Xiao, F., Liu, X. & Guo, S. W. Platelets and regulatory T cells may induce a type 2 immunity that is conducive to the progression and fibrogenesis of endometriosis. *Front. Immunol.* **11**, 610963 (2020).
47. Stratton, M. S. et al. Dynamic chromatin targeting of BRD4 stimulates cardiac fibroblast activation. *Circ. Res.* **125**(7), 662–677 (2019).
48. Han, X. et al. Heterogeneity of clinical symptoms and therapeutic strategies for different subtypes of adenomyosis: An initial single-center study in China. *Int. J. Gynaecol. Obstet.* **161**(3), 775–783 (2023).
49. Rossi, M. et al. Mechanisms and pathogenesis of adenomyosis. *Curr. Obstet. Gynecol. Rep.* **11**(2), 95–102 (2022).
50. Dason, E. S. et al. Guideline No. 437: Diagnosis and management of adenomyosis. *J. Obstet. Gynaecol. Can.* **45**(6), 417-429.e1 (2023).
51. van Straalen, K.R. et al. Single-cell sequencing reveals Hippo signaling as a driver of fibrosis in hidradenitis suppurativa. *J. Clin. Investig.* **134**(3) (2024).
52. Chen, Y. et al. SFRP4(+)IGFBP5(hi) NKT cells induced neural-like cell differentiation to contribute to adenomyosis pain. *Front. Immunol.* **13**, 945504 (2022).
53. Yildiz, S. et al. Adenomyosis: single-cell transcriptomic analysis reveals a paracrine mesenchymal-epithelial interaction involving the WNT/SFRP pathway. *Fertil. Steril.* **119**(5), 869–882 (2023).
54. Stallone, G. et al. Coagulation and fibrinolysis in kidney graft rejection. *Front. Immunol.* **11**, 1807 (2020).
55. Long, Y. et al. Mechanical communication in fibrosis progression. *Trends Cell Biol.* **32**(1), 70–90 (2022).
56. Chen, C. et al. Ganoderma lucidum polysaccharide inhibits HSC activation and liver fibrosis via targeting inflammation, apoptosis, cell cycle, and ECM-receptor interaction mediated by TGF-beta/Smad signaling. *Phytomedicine* **110**, 154626 (2023).
57. Troilo, H. et al. Independent multimerization of Latent TGFβ Binding Protein-1 stabilized by cross-linking and enhanced by heparan sulfate. *Sci. Rep.* **6**(1), 34347 (2016).
58. Demonbreun, A. R. et al. Anti-latent TGFβ binding protein 4 antibody improves muscle function and reduces muscle fibrosis in muscular dystrophy. *Sci. Transl. Med.* **13**(610), eabf0376 (2021).
59. Tokarz, J., Adamski, J. & Rizner, T. L. Metabolomics for diagnosis and prognosis of uterine diseases? A systematic review. *J. Pers. Med.* **10**(4), 294 (2020).

Acknowledgements

We thank Xiantaoxueshu (http://www.xiantao.love) for their invaluable data visualization and support in statist ical analysis. Additionally, we thank the Citexs website (http://www.citexs.com) for their assistance with editing the English language.

Author contributions

Qiaomei Yang contributed to the design, methodology, and manuscript drafting. Jianhui Fu and Jingxuan Hong analyzed the data and drafted the manuscript. Xianhua Liu, Xinye Zheng and Hao Lin contributed to the data collection and editing. Li Chen, Junying Jiang and An Zhu designed the study and conducted the statistical analysis. Pengming Sun supervised the study and contributed to the design and review of a manuscript. All authors approved the submitted version and agreed to be accountable for all aspects of the work.

Funding

This study was supported by Fujian Provincial Natural Science Foundation of China (Grant NO.2023J011216); Joint Funds for the Innovation of Science and Technology of Fujian Province (Grant NO.2023Y9391); Fujian Provincial Health Technology Project (Grant NO.2023CXA039).

Declarations

Ethics approval and consent to participate

This study adhered to the Declaration of Helsinki regarding Human Research Ethics and received approval from the Ethics Committee of Fujian Maternal and Child Health Hospital (Approval No. 2023KYLLRD01030). Patients' privacy was rigorously protected, ensuring the confidentiality of their personal information. Patient-identifiable information is concealed when data are presented.

Competing interests
The authors declare no competing interests.

Additional information
Supplementary Information The online version contains supplementary material available at https://doi.org/10.1038/s41598-025-98369-2.

Correspondence and requests for materials should be addressed to P.S.

Reprints and permissions information is available at www.nature.com/reprints.

Publisher's note Springer Nature remains neutral with regard to jurisdictional claims in published maps and institutional affiliations.